Long-Lived Mesoconvective Vortices and Their Environment. Part II: Induced Thermodynamic Destabilization in Idealized Simulations

S. B. TRIER, C. A. DAVIS, AND W. C. SKAMAROCK

*National Center for Atmospheric Research, Boulder, Colorado**

(Manuscript received 10 September 1999, in final form 9 February 2000)

ABSTRACT

Idealized numerical simulations are used to quantify the effect of quasi-balanced lifting arising from the interaction of the ambient vertical shear with midtropospheric cyclonic vortices (MCVs) generated by mesoscale convective systems on thermodynamic destabilization over a range of ambient vertical shear strengths and vortex characteristics observed in Part I. Maximum upward displacements occur beneath the midtropospheric potential vorticity anomaly, near the radius of maximum tangential vortex winds. The location of the region of upward displacements relative to the ambient vertical shear vector depends on the relative strength of the vortex tangential flow and the ambient vertical shear, and ranges from downshear for vortices of moderate strength in strong ambient vertical shear to 90° to the left of downshear for strong vortices in weak ambient vertical shear. Although significant upward displacements occur most rapidly with small vortices in strong ambient vertical shear, maximum upward displacements are associated with large vortices and occur in approximately average vertical shear for MCV environments.

The simulations suggest that in larger and stronger than average MCVs, the lifting that results from the MCV being embedded in a weakly baroclinic environment is, alone, sufficient to saturate initially moist and conditionally unstable layers immediately above the boundary layer. The horizontal location of the resulting thermodynamic instability is approximately coincident with the maximum lower-tropospheric upward displacements. Since in the absence of sustained deep convection the vortices develop substantial vertical tilt, the destabilized region in the lower troposphere lies nearly underneath the vortex center at its level of maximum strength, consistent with observations that redevelopment of organized, long-lived (e.g., $t \geq 6$ h) deep convection is most often found near the midtropospheric MCV center. This location for convectively induced stretching of preexisting vertical vorticity is optimal for maintaining the vortex against the deleterious effect of differential advection by the ambient shear.

1. Introduction

Part I of this study (Trier et al. 2000) presented observations of midtropospheric cyclonic vortices (MCVs) generated by mesoscale convective systems (MCSs) that occurred over the central United States from 15 May to 15 September 1998. These observations indicated that long-lived MCVs, which persist from several hours to several days past the decay of the MCSs from which they were spawned, occur in weaker ambient vertical shear than that found in typical MCS environments, and may be more common than previously suspected. Both observations from Part I and those from previous studies (e.g., Bartels and Maddox 1991) have shown that organized secondary (i.e., subsequent) convection forms either within, or in close proximity to, MCVs in about 1/2 of long-lived MCV cases.

Long-lived MCVs are quasi-balanced circulations (Raymond and Jiang 1990; Davis and Weisman 1994). Despite their relatively small horizontal scale (e.g., 50–250 km), they are coherent and nondispersive structures that, once formed, are likely to be highly predictable. Thus, much of the interest in MCVs hinges on the possibility that the secondary convection forced by MCVs may itself be more predictable than other forms of deep atmospheric convection. In the current study we use numerical simulations with a primitive equation (PE) model to investigate the behavior of idealized vortices that resemble MCVs.

Mesoscale lifting associated with balanced vortices in vertical shear has been illustrated in previous numerical studies (e.g., Raymond and Jiang 1990; Raymond 1992; Jones 1995; Frank and Ritchie 1999). Herein, we quantify how the lifting arising from interaction of the vortex with the ambient vertical shear can modify the thermodynamic structure in weakly baroclinic MCV

* The National Center for Atmospheric Research is sponsored by the National Science Foundation.

Corresponding author address: Dr. Stanley B. Trier, NCAR/MMM, P.O. Box 3000, Boulder, CO 80307-3000.
E-mail: trier@ucar.edu

environments representative of those observed in Part I. While our analysis is applied to MCV-like circulations, the dynamics are balanced and in principle could represent aspects of behavior in other types of balanced circulations such as tropopause-based (e.g., nonconvective) short wavelength disturbances.

Several unresolved issues that are fundamental to understanding the role of the vortex–ambient shear interaction mechanism in the development of secondary convection in the vicinity of MCVs are addressed. In particular, we examine where, relative to the MCV center, significant thermodynamic destabilization associated with this lifting mechanism is likely to occur, and to what extent it explains distributions of secondary convection in observed MCVs. We also examine how the magnitude of the lifting depends on vortex characteristics, including intensity, horizontal scale, and vertical structure. Since the ambient vertical shear may contribute positively to mesoscale lifting through its interaction with the vortex, but negatively to vortex strength and longevity through differential advection, we investigate whether there is some optimal value of shear for which this lifting mechanism can act most effectively.

Section 2 briefly summarizes the numerical model we use and describes the initialization of idealized vortices in vertically sheared basic states. We also discuss the design of several sets of numerical simulations aimed at addressing the issues raised in the previous paragraph. Section 3 describes the evolution of a vortex and its associated thermodynamic structure from a control simulation based on an observed MCV that was associated with multiple long-lived episodes of secondary convection. In section 4, we examine the influence of initial vortex characteristics and the ambient vertical shear on the mesoscale lifting and associated thermodynamic destabilization in the vicinity of the idealized vortices. Results are summarized in section 5 and discussed within the context of the observations of MCVs presented in Part I.

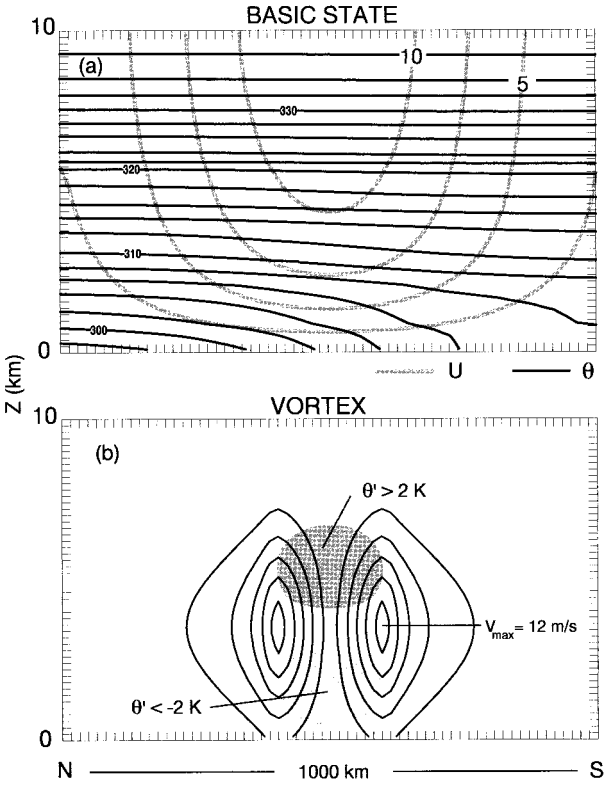

FIG. 1. Initial conditions for the control simulation V2R3S2. North–south cross section of (a) basic-state potential temperature (dark contours, 2-K increments) and zonal wind (light contours, 2.5 m s^{-1} increments, zero contour omitted) in thermal wind balance and (b) tangential wind (2 m s^{-1} contour intervals) with easterly (westerly) flow north (south) of the vortex center, and the associated balanced potential temperature perturbation ($\theta' \leq -2$ K, light shading; $\theta' \geq 2$ K, dark shading) superposed on the basic state in (a).

2. Methodology

a. Numerical model

The three-dimensional PE model used in this study was described by Wicker and Wilhelmson (1995). The current simulations utilize a single computational grid and do not allow water vapor to change phase. This approach allows us to follow the evolution of potential temperature, θ, and specific humidity, q_v, to determine where the interaction of the vortex circulation with the ambient vertical shear would be likely to produce moist convection but, as in strictly dry simulations, does not allow the complicating effects of moist convection and its associated latent heat release to occur. In addition to θ and q_v, the prognostic variables include the three wind components u, v, and w; the Exner function (nondimensional pressure) π; and an initially horizontally homogeneous passive scalar that allows determination of vertical parcel displacements.

b. Initialization

To initialize simulations, an axisymmetric vortex in gradient balance is superimposed on a thermally balanced vertically sheared flow that is zonally invariant (Fig. 1). While both the vortex and the basic-state zonal jet are balanced, the superposition of these flows is not a steady solution to the equations of motion. However, model initialization with this idealized flow provides a simple framework in which to examine the effect of ambient shear on vortex evolution and does not produce large-amplitude inertia–gravity waves, which would complicate interpretation.

In addition to a midtropospheric cyclonic vortex, surface and upper-tropospheric anticyclones are commonly observed in the wake of MCSs (e.g., Maddox 1983; Cotton et al. 1989). Unlike the midtropospheric vortex, these anticyclonic circulations are highly divergent and less steady. While the MCS-induced surface anticy-

clone, in particular, may influence the location and timing of secondary convection along its cold outflow boundary, the lifting it provides is largely independent from the background lifting associated with the vortex. Moreover, the shallow cold surface anticyclone is often eroded by daytime surface heating. For simplicity, these anticyclonic circulations are not included in our idealized simulations.

The thermally balanced potential temperature distribution associated with the basic-state zonal jet has the form

$$\theta(y, z) = \overline{\theta}(z) - \Delta\theta \tanh\left(a_y \frac{y}{L}\right) \exp\left(-a_z \frac{z}{D}\right), \quad (1)$$

where the amplitude of the frontal potential temperature perturbation, $\Delta\theta$, and the horizontal, L/a_y, and vertical, D/a_z, decay scales of the baroclinic zone are chosen (section 2c) to produce a range of thermally balanced vertical shears representative of those observed in MCV environments described in Part I. Here, y and z are the distances from the N–S domain center and above ground level, respectively. The frontal temperature gradient and associated vertical shear is strongest at the surface, at the N–S domain center (Fig. 1a). Since we assume constant D/a_z and L/a_y, the only variation in the basic state among simulations is in the amplitude, $\Delta\theta$, of the baroclinic zone and associated vertical shear.

Surface friction is neglected in the current simulations. In actual cases, surface friction disrupts the thermal wind balance. The assumption of thermal wind balance in the current simulations allows for a steady background flow, which facilitates interpretation of the interaction of the vortex with the ambient shear. Since the vortex resides primarily above the boundary layer and its intensity within the boundary layer is weak, neglected effects of frictional convergence on the evolution of the vortex flow are likely to be small. However, in some cases the lower-tropospheric vertical motion associated with the secondary circulation induced by friction (Ekman pumping) may not be negligible in comparison to the vortex-induced lifting, particularly during the early stages of simulations. This issue is discussed further in section 3a.

The horizontally independent part of the basic-state potential temperature, $\overline{\theta}(z)$, is based on a composite of two soundings obtained downshear of the vortex circulation of the series MCV case of 27–29 May 1998. This case comprised several long-lived episodes of secondary convection and is described in section 5 of Part I. Soundings from Little Rock, Arkansas (LZK), at 0000 UTC 28 May and from Jackson, Mississippi (JAN), at 0000 UTC 29 May (Table 2 of Part I) were used to construct the composite sounding in a manner identical to that described in section 2c of Part I. This composite sounding (Fig. 2) has convective available potential energy (CAPE) of ~2000 J kg^{-1} and convective inhibition (CIN) of ~50 J kg^{-1} for pseudoadiabatic ascent of air parcels averaged through the lowest 500 m.[1]

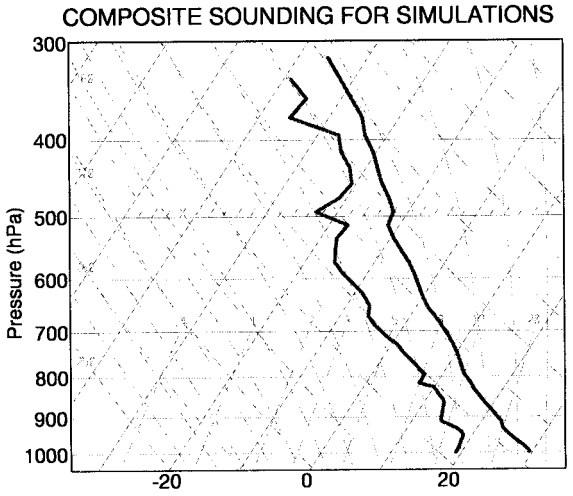

FIG. 2. Composite sounding from the environment of the 27–29 May 1998 case used to supply the horizontally independent part of the initial thermodynamic vertical structure for all simulations.

The sensitivity of MCV evolution in these dry simulations to typical variations in warm-season $\overline{\theta}(z)$ profiles is small. Our choice of sounding is motivated by the desire to illustrate the effects of the MCV circulation on thermodynamic destabilization in environments known to support prolonged secondary convection. The vertical profile of q_v is also specified by the composite sounding (Fig. 2). A major simplification of the current study is that while θ varies initially in the horizontal due to the separately balanced frontal and vortex potential temperature perturbations, we assume that q_v is initially horizontally homogeneous.[2]

The vortex superimposed on the meridional frontal zone and associated zonal jet has the tangential flow

$$V(r, z) = \begin{cases} b(z)V_m\left(\dfrac{r}{r_m}\right), & r \le r_m \\ b(z)V_m\left(\dfrac{r_m}{r}\right)^c, & r \ge r_m, \end{cases} \quad (2)$$

wherein r is the distance from the vortex center, which

[1] The potential temperature, $\overline{\theta}(z)$, over the lowest 1.5 km was modified slightly from the composite sounding ($\le$1 K at any given level) to ensure positive static stability in the vicinity of the vortex after both the baroclinic basic-state and vortex temperature perturbations were superimposed. These changes resulted in small reductions in CAPE from the composite sounding (Fig. 2) of order 200 J kg^{-1}, with insignificant changes in CIN.

[2] Since the current simulations are adiabatic, the effect of the specified moisture field is negligible. We retain a simple moisture field to illustrate to extent to which quasi-balanced lifting can influence the evolution of thermodynamic stability. In actual cases details of this evolution will depend on the more complicated inhomogeneous vertical thermodynamic structure.

itself is located at the center of the horizontal domain, V_m is the maximum tangential wind within the vortex, r_m is the distance of the maximum wind from the vortex center, and the Coriolis parameter $f = 10^{-4}$ s^{-1}. By specifying $c = 1 + fr_m/V_m$, absolute vertical vorticity, $(\zeta + f)$, is ≥ 0 for all r. The vortex has the vertical structure

$$b(z) = \exp\left[\frac{-(z - z_m)^2}{2H^2}\right], \tag{3}$$

wherein H is its Gaussian half-depth, z is height above the surface, and z_m is the height of V_m. The balanced vortex potential temperature perturbation is

$$\theta'(r, z) = \frac{c_p \overline{\theta}(z)^2}{g} \frac{\partial \pi'}{\partial z}, \tag{4}$$

wherein $c_p = 1004$ J kg^{-1} is the specific heat at constant pressure, $g = 9.81$ m s^{-1} is gravity, and the perturbation Exner function

$$\pi'(r, z) = \begin{cases} \dfrac{-V_m b(z)}{c_p \overline{\theta}(z)} \left[\dfrac{V_m b(z)}{2} \left(1 + \dfrac{1}{c} - \dfrac{r^2}{r_m^2} \right) + f \left(\dfrac{r_m}{c - 1} + \dfrac{r_m}{2} - \dfrac{r^2}{2r_m} \right) \right], & r \leq r_m \\ \dfrac{-V_m b(z)}{c_p \overline{\theta}(z)} \left[\dfrac{V_m b(z)}{2c} \left(\dfrac{r_m}{r} \right)^{2c} + \dfrac{f r_m^c r^{1-c}}{c - 1} \right], & r \geq r_m \end{cases} \tag{5}$$

is obtained from a radial integration of the gradient wind equation.

Figure 1b illustrates the initial vortex flow, V, and its balanced θ' perturbation for the control simulation described in section 3. The analytic formulation (2)–(5) used for all vortices in the simulations (section 2c), which includes an $(r_m/r)^c$ dependence of V in the outer core of the vortex ($r \geq r_m$), and solid-body rotation, $V \propto r$, in the inner core ($r \leq r_m$), ensures a finite pressure perturbation, π', for all r.

c. Range of experiments

The simulations are designed to examine the vortex evolution and thermodynamic destabilization brought about by the interaction of the vortex circulation with ambient vertical shear over an observed range of ambient vertical shear strength and vortex characteristics. All simulations are performed in a domain of depth $D = 16$ km, with a vertical grid spacing of $\Delta z = 200$ m. The horizontal and vertical frontal decay scales used in (1) are $L/a_y = 450$ km and $D/a_z = 2.2$ km, respectively.

The primary set of experiments comprises two 3×3 matrices of simulations (Table 1), with $V_m = 12$ m s^{-1} representative of MCVs of greater than average strength and $V_m = 8$ m s^{-1} representative of MCVs of average strength[3] (cf. Fig. 4, Part I). For both matrices, the individual rows contain simulations in which the vortices have identical r_m of either 25, 50, or 100 km, and the columns each contain simulations in which the background baroclinic zone has identical $\Delta\theta$ of either 3.175, 6.350, or 9.525 K. Table 2 lists the frontal ($\Delta\theta$) and vortex (V_m, r_m) parameters that vary for these simulations. Also listed are the horizontal model domain sizes $2L$ and horizontal grid spacings, $\Delta x, y$ (which are each varied with specified r_m), and the domain translation speeds, c (which are varied with specified $\Delta\theta$).

The constant D/a_z and the median value of $\Delta\theta = 6.350$ K in (1) are selected to yield values of 2.90×10^{-3} s^{-1} and 1.10×10^{-3} s^{-1} for the respective values of 0.5–2.5- and 2–6-km vertical shear at the N–S center of the model domain (Table 2). These values of vertical shear are based on the lower- and midtropospheric ambient vertical shears in MCV environments observed in Part I, but are reduced to account for the constraint of unidirectional vertical shear in the current simulations.[4] The $\Delta\theta$ values in the first and third columns of the simulation matrices (Table 1) result in vertical shears (Table 2) that are one-half and twice the strength of these reduced average vertical shear magnitudes, and together constitute a realistic range of MCV ambient vertical shear magnitudes for the current idealized modeling framework.

The parameters $z_m = 3.5$ km and $H = 2$ km determine the initial location of the vortex center in the vertical and the vertical decay of the vortex from its center (3), and are identical for all simulations contained in these two matrices. The values of these parameters are chosen

[3] Our use of the terminology ''vortex strength'' refers to the magnitude of its maximum tangential wind, V_m. Local values of maximum relative vorticity for vortices with identical V_m are largest in vortices with smaller radii of maximum tangential wind, r_m.

[4] Constructing a unidirectional vertical shear profile by simply superposing the magnitudes of lower-tropospheric and midtropospheric vertical shear from the observed *three-dimensional* vertical shear profiles of Part I would likely result in unrealistically large rates of differential advection of the vortex.

TABLE 1. Listing of numerical simulations with constant vortex vertical structure parameters $H = 2$ km, $z_m = 3.5$ km, and variable strength of baroclinity (vertical shear) $\Delta\theta$ and vortex horizontal scale r_m for moderate ($V_m = 8$ m s^{-1}) and strong (12 m s^{-1}) vortices.

V_m (m s^{-1})	r_m (km)	Baroclinity [$\Delta\theta$ (K)] 3.175	6.350	9.525
8	25	V1R1S1	V1R1S2	V1R1S3
8	50	V1R2S1	V1R2S2	V1R2S3
8	100	V1R3S1	V1R3S2	V1R3S3
12	25	V2R1S1	V2R1S2	V2R1S3
12	50	V2R2S1	V2R2S2	V2R2S3
12	100	V2R3S1	V2R3S2	V2R3S3

to best replicate the vertical structure of the balanced (rotational) flow associated with an MCV that developed in a high-resolution simulation of deep convection (Skamarock et al. 1994). That simulation was initialized using an analytic basic state similar to (1), in which there was also a zonal jet with the strongest vertical shear concentrated in the lower troposphere, beneath the vortex center.

The influence of the vertical structure of the vortex on subsequent thermodynamic destabilization in its vicinity is examined in an additional set of simulations (Table 3). These experiments focus on vortex and environmental initial conditions for which vortices are most susceptible to strong thermodynamic destabilization (section 4) and include only vortices occurring in median vertical shear ($\Delta\theta = 6.350$ K) that are both stronger ($V_m = 12$ m s^{-1}) and larger ($r_m = 100$ km) than average. Among these experiments are the control simulation V2R3S2 (Tables 1 and 2) and two other experiments wherein the vertical scale of the vortex is varied from $H = 2$ km (control) to a deeper vortex with $H = 2.5$ km (V2R3S2D) and a shallower vortex with $H = 1.5$ km (V2R3S2S), with no change in any of the other parameters. In the final experiment of this set (V2R3S2H), the vertical scale of the vortex is the same as in the control simulation, but the vortex center is raised from $z_m = 3.5$ km to $z_m = 5.5$ km.

TABLE 3. Parameters for simulations with variable vertical structure. All other parameters are listed under the control simulation V2R3S2 in Table 2.

Simulation	z_m (km)	H (km)
V2R3S2S	3.5	1.5
V2R3S2	**3.5**	**2.0**
V2R3S2D	3.5	2.5
V2R3S2H	5.5	2.0

3. Control simulation

The choice of environmental and vortex parameters for the control simulation (V2R3S2, Table 2) is based on the early stages of the 27–29 May case discussed in section 5 of Part I. This MCV was the largest and one of the strongest MCVs in the 1998 sample. Of the three ambient vertical shear/baroclinic zone strengths for the matrices of simulations (Table 1), we use the median value of 6.350 K since it most closely approximates observations downshear of the observed MCV. It was hypothesized in Part I that the secondary convection that persisted overnight (after 0000 UTC on 28 May) near the center of the MCV was strongly forced by mesoscale lifting associated with the interaction of the MCV circulation with the ambient vertical shear. In this section we examine this hypothesis by following the evolution of both the idealized vortex and its associated thermodynamic vertical structure.

TABLE 2. Parameters for the two simulation matrices (Table 1) with variable ambient shear and vortex size. Each simulation has the vertical structure parameters $z_m = 3.5$ km and $H = 2$ km. Parameters for the control simulation are listed in boldface.

Simulation	V_m (m s^{-1})	r_m (km)	$\Delta\theta$ (K)	Vertical shear (10^{-3} s^{-1}) 0–2.5 km	2–6 km	$2L$ (km)	$\Delta x, y$ (km)	c (m s^{-1})
V1R1S1	8	25	3.175	1.45	0.55	400	4	4.0
V1R1S2	8	25	6.350	2.90	1.10	400	4	7.5
V1R1S3	8	25	9.525	4.35	1.65	400	4	11.0
V1R2S1	8	50	3.175	1.45	0.55	800	8	4.0
V1R2S2	8	50	6.350	2.90	1.10	800	8	7.5
V1R2S3	8	50	9.525	4.35	1.65	800	8	11.0
V1R3S1	8	100	3.175	1.45	0.55	1600	16	4.0
V1R3S2	8	100	6.350	2.90	1.10	1600	16	7.5
V1R3S3	8	100	9.525	4.35	1.65	1600	16	11.0
V2R1S1	12	25	3.175	1.45	0.55	400	4	4.0
V2R1S2	12	25	6.350	2.90	1.10	400	4	7.5
V2R1S3	12	25	9.525	4.35	1.65	400	4	11.0
V2R2S1	12	50	3.175	1.45	0.55	800	8	4.0
V2R2S2	12	50	6.350	2.90	1.10	800	8	7.5
V2R2S3	12	50	9.525	4.35	1.65	800	8	11.0
V2R3S1	12	100	3.175	1.45	0.55	1600	16	4.0
V2R3S2	**12**	**100**	**6.350**	**2.90**	**1.10**	**1600**	**16**	**7.5**
V2R3S3	12	100	9.525	4.35	1.65	1600	16	11.0

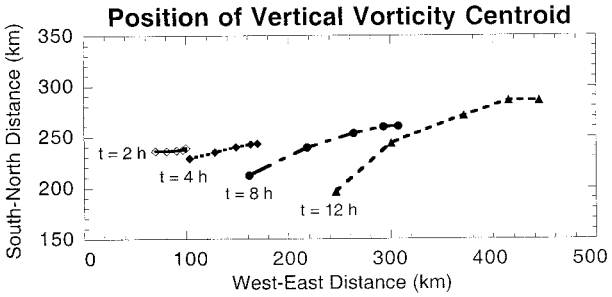

FIG. 3. Location (in a fixed ground-relative coordinate system) of the centroid of the smoothed vertical component of relative vorticity (see text for details) in the control simulation V2R3S2 at 1-km height intervals (symbols) from 1.5 to 5.5 km AGL at $t = 2$, 4, 8, and 12 h.

a. Vortex evolution

A vortex placed in ambient vertical shear will begin to tilt downshear due to its differential advection by the shear. The vertical tilt of the vortex in the current simulation is quantified using amplitude-weighted centroids of the vertical component of relative vorticity, $\Sigma_i \zeta_i' r_i(\Sigma_i \zeta_i')^{-1}$, wherein ζ_i' is the relative vorticity at grid points i with the contribution from the basic-state N–S baroclinic zone subtracted out, and r_i is the distance of grid points from some reference location. The perturbation relative vorticity, ζ', is initially axisymmetric. However, the vortex perturbation develops asymmetries (not shown), due in part to its divergent secondary circulation that develops within the vertically sheared environment (e.g., Jones 1995). The amplitude-weighted centroids of relative vorticity are less affected by these temporally varying asymmetries than are locations of relative vorticity maxima and, thus, better describe the vertical tilt of the large-scale circulation associated with the vortex.

Aspects of the evolution of vortex tilt resemble those found by Jones (1995) for simulated tropical cyclone vortices that were initially barotropic and embedded within a constant vertical shear. The vertical tilt is initially downshear, but becomes oriented to the left of the ambient vertical shear vector as the vortex centers at 1.5 and 5.5 km become displaced to the south and north, respectively (Fig. 3). By 12 h the horizontal separation of the 1.5- and 5.5-km, centers is 192 km, which is 39 km less than the separation that occurs solely from differential advection by the ambient vertically sheared flow.

Jones (1995) attributed the cyclonic rotation of upper- and lower-level centers to circulations induced by the vertical penetration of these potential vorticity (PV) anomalies as they become horizontally displaced from each other. She also found that the divergent secondary circulation augmented the rotation of the PV centers and the related reduction in the magnitude of the vertical tilt of the vortex from that which would occur if the differential advection was the only mechanism operating to alter vertical tilt. These additional influences on vortex tilt, while present, are considerably weaker in the current simulation. This is consistent with the vortex, itself, being several times weaker and the ambient vertical shear being several times stronger than in the simulations of tropical cyclone vortices. The magnitude of the ambient vertical shear varies with height in the current simulations (Table 2), which is reflected in the stronger tilt of the vortex in the lower troposphere (beneath 3 km) than in the middle troposphere (Fig. 3).

In the early stages of the simulation lower-tropospheric ascent occurs on the downshear (eastern) edge of the vortex with descent on the upshear (western) edge (Fig. 4a). This is consistent with the theory of Raymond and Jiang (1990), which predicts a similar vertical motion pattern arising from both the motion associated with the ambient shear along isentropic surfaces deformed by the vortex (Fig. 2a of Part I) and vortex-induced motion along the isentropic surfaces that compose the ambient baroclinic zone (Fig. 2b of Part I). Time series (Fig. 5) reveal a rapid increase in maximum vertical velocity from zero at the start of the simulation to relatively steady values of 3–3.5 cm s^{-1} by 1 h at 3 km, and from 0 to 5–5.5 cm s^{-1} by 2 h at 1.5 km. After the initial increase in vertical motion, the orientation of the vertical motion couplet at 3 km shifts in the anticyclonic direction from downshear at 1 h (Fig. 4a) to 60° to the right of downshear (Fig. 4b) by 8 h, with little further adjustment thereafter. An anticyclonic rotation of the vertical velocity couplet also occurs at 1.5 km (not shown). However, at 1.5 km, this adjustment does not become apparent until ~2 h and remains less pronounced than at 3 km.

The lifting mechanism of Raymond and Jiang (1990) applies to a steady vortex in ambient shear. While this mechanism is consistent with the lower-tropospheric vertical motion pattern during the early stages of the simulation, it cannot account for the anticyclonic rotation of the vertical velocity couplet. Raymond (1992) noted that the vertical velocity is also influenced by time-dependent evolution of isentropic surfaces arising from shear-induced changes in the PV distribution. As the vortex acquires vertical tilt, in order to remain balanced, its negative and positive potential temperature anomalies must lie beneath and above the PV anomaly, respectively, as illustrated by Jones (1995, her Fig. 4b).

Similar to the findings of Reasor et al. (2000), the evolution of the vertical motion pattern in the current case is qualitatively consistent with expectations from quasigeostrophic theory, despite a relatively large Rossby number, $\mathrm{Ro} \equiv V_m(fr_m)^{-1}$, of 1.2. Herein, this is demonstrated by considering the quasigeostrophic forcing associated with vorticity advection by the thermal wind. In the early stages of the simulation, the circulation center and negative potential temperature anomaly are nearly collocated (Fig. 4a). In this configuration the advection of vertical vorticity is largely by the ambient (westerly) thermal wind, consistent with the orientation of the vertical motion couplet along the ambient vertical

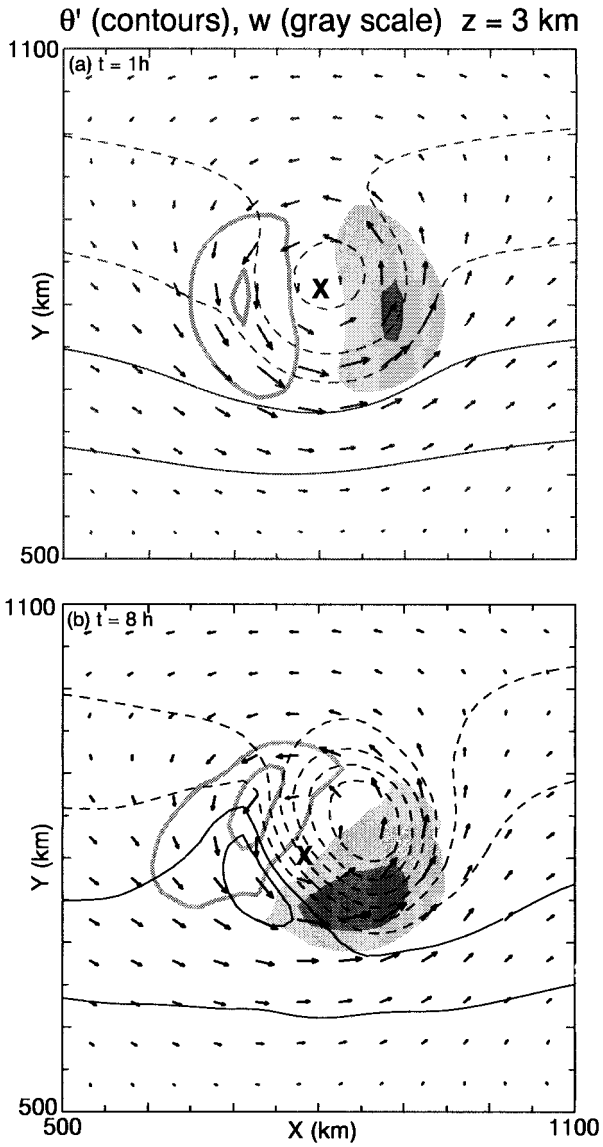

FIG. 4. The 3-km AGL system-relative flow vectors, potential temperature perturbation (contour intervals of 0.5 K, negative values dashed), and vertical velocity [shaded for $w \geq 1$ cm s^{-1} (light), $w \geq 3$ cm s^{-1} (dark) and contoured in gray for $w = -1$ and -3 cm s^{-1}] at (a) 1 and (b) 8 h for the control simulation V2R3S2. The centroid of the vertical component of relative vorticity is indicated by the symbol ×. Vectors are plotted at every third model grid point. A vector the length of the spacing between tick marks has the magnitude of 15 m s^{-1}.

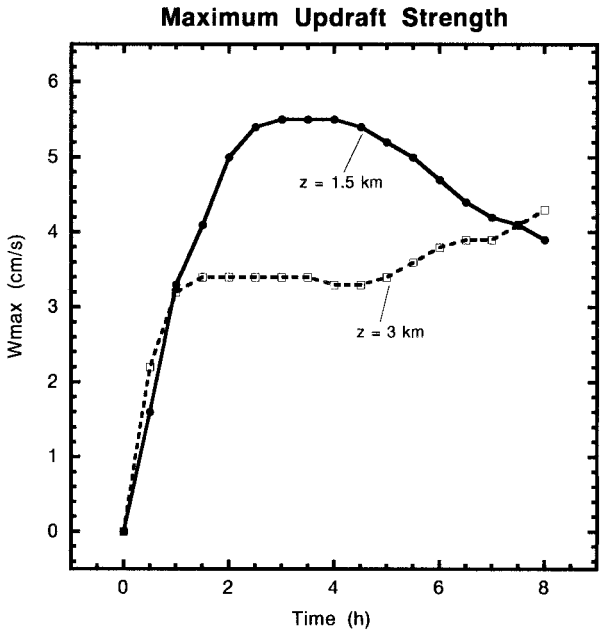

FIG. 5. Time series of maximum vertical velocity at 1.5 (solid) and 3 km (dashed) AGL for the control simulation V2R3S2.

shear vector (Fig. 4a). In order for the vortex to remain balanced as it acquires vertical tilt, its associated negative temperature anomaly becomes significantly displaced from the center of circulation in the direction of the vortex tilt (Fig. 4b). By this stage of evolution, a strong potential temperature gradient is situated over the center of circulation, oriented antiparallel to the axis of vortex tilt. Here, positive (negative) advection of vertical vorticity by the thermal wind, resulting from the displacement of the cold potential temperature anomaly from the circulation center, is consistent with the ascent (descent) on the southeast (northwest) flank of the vortex.

Frank and Ritchie (1999) found that effect of Ekman pumping (neglected in the current simulations) on vertical velocity within the boundary layer (i.e., at 950 mb) was comparable to that of balanced lifting resulting from the interaction of vortex with ambient vertical shear. In their simulations, frictionally induced ascent augmented that of the balanced lifting when the movement of the vortex was in the direction of the vertical shear, which was typically the case for the MCVs observed in Part I. However, unlike in the current case, Frank and Ritchie investigated vortices representative of developing tropical cyclones, in which the ambient lower-tropospheric vertical shear was an order of magnitude weaker than in the current simulations. Since stronger ambient vertical shear will engender stronger balanced lifting, for a diffusivity similar to that used by Frank and Ritchie, we would expect this effect to dominate that of Ekman pumping for the current MCV simulations.

b. Vertical displacements

Mesoscale regions of vertical displacement, which result from the time-integrated effect of the evolving vertical and horizontal motions, govern the thermodynamic destabilization in the vicinity of the vortex. Although the maximum vertical motions associated with the interaction of the vortex with the ambient shear are only on the order of ~5 cm s^{-1}, the lifting is persistent (Fig. 5) and widespread (Fig. 4). Maximum upward displacements occur in the lower troposphere around 1.5 km.

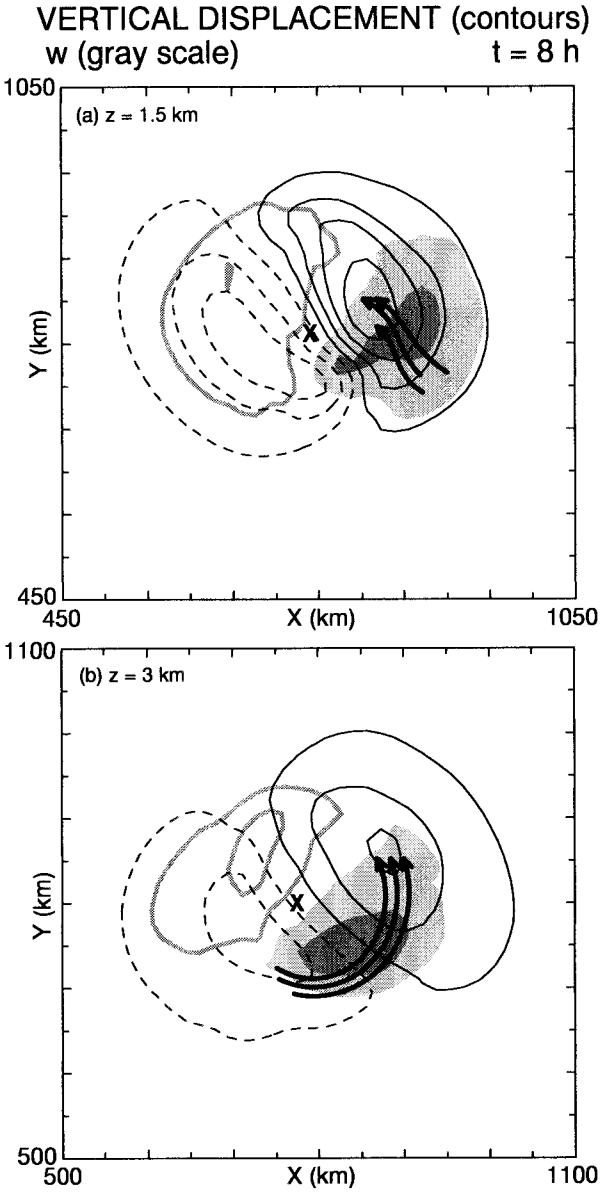

FIG. 6. The 8-h vertical displacement field [contoured every 200 m starting at 100 m (positive values solid) and −100 m (negative values dashed)] with 8-h back trajectories from the region of strong upward displacement at (a) 1.5 and (b) 3 km AGL in the control simulation V2R3S2. Indication of the centroid of the vertical component of relative vorticity and the gray shading and contouring of vertical velocity are as in Fig. 4.

At 8 h these upward displacements are located on the northeast flank of the vortex and exceed 800 m (Fig. 6a), which means that air present at 1.5 km at 8 h originates from as low as 700 m, within the undisturbed boundary layer.

Trajectory calculations establish the horizontal source region of the air that undergoes the strongest vertical displacements. Following Weisman and Klemp (1984), we calculate time-dependent trajectories using model output every 30 min and a 1-km extrapolation interval. Back trajectories from the maximum upward displacement region at 1.5 km (Fig. 6a) originate from the southeastern periphery of the vortex. Owing to the ambient vertical shear, these low-level trajectories have a strong radial component of horizontal velocity as they are entrained into the core of the vortex circulation. In contrast, the back trajectories from the region of maximum upward displacement at 3 km (Fig. 6b) originate at a level where the tangential vortex flow is strong and the ambient flow relative to the vortex motion is weak. The maximum upward displacements at both levels occur after air has traveled through the vertical velocity anomaly, with differences in location of the maximum displacements relative to the vertical motion pattern dependent on the character of the trajectories.

The magnitudes and locations of maximum upward displacements differ from those that would occur in a steady vortex with negligible vertical tilt. Recall that by 1 h maximum 3-km vertical velocity has reached relatively steady magnitudes (Fig. 5) but has not yet shifted anticyclonically from its position downshear of the vortex center (Fig. 4a). Taking the kinematic structure of the vortex at this time and assuming steady conditions yields maximum 8-h upward displacements at 3 km (not shown) that exceed the simulated upward displacements by 115 m (22%), and are located directly north of the vortex center, rather than on the northeastern flank (Fig. 6b). These differences are consistent with the lack of a shear-induced shift in the region of upward motion in the hypothetical steady case. In the nonsteady case, upwardly displaced air parcels spend less time in regions of significant upward motion since the region of instantaneous upward motion rotates southward (anticyclonically), opposite to the northward horizontal component of the air parcel trajectories (cf. Figs. 4 and 6b). Differences between the hypothetical steady case and simulated nonsteady cases are substantially less for upward displacements at 1.5 km, below which the anticyclonic rotation of the instantaneous vertical motion couplet is less pronounced.

c. Thermodynamic destabilization associated with the vortex circulation

We now examine how the vortex circulation interacting with the ambient vertical shear can thermodynamically destabilize the environment in the vicinity of the vortex. There are two basic means by which destabilization can be achieved. The CAPE for a given layer can be raised by some combination of lifting and advective change of equivalent potential temperature, θ_e, within the layer itself or by potential temperature changes within the column overlying the layer. Initiation of deep convection from conditionally unstable layers (i.e., those in which CAPE > 0) is more likely to occur when the negative buoyancy between the source levels of air parcels within the layer and their level of free convection

(LFC) is decreased. For surface-based air parcels, this reduction in negative buoyancy results in a decrease of CIN. In the second case, absolute thermodynamic instability will occur when the vertical and/or horizontal displacements are sufficient to saturate a conditionally unstable layer. Only in the second case is additional forcing not required to release the instability.

We begin by examining the thermodynamic evolution of the boundary layer, which contains the most unstable (i.e., high θ_e) air (Fig. 2). We focus on the period from 0 to 8 h when strong vertical displacements occur. Superposed on $\overline{\theta}(z)$ and q_v from the initial sounding (Fig. 2) are horizontal gradients of θ, of which there is a northward component associated with the balanced jet–front structure and an additional component that extends radially outward from the vortex center in association with its balanced potential temperature perturbation. Hence, in addition to vertical advections, horizontal advections contribute strongly to the evolution of thermodynamic vertical structure.

Changes in CIN (for air parcels averaged over the lowest 500 m) for the 8-h period are calculated relative to the vortex position at 1.5 km above ground level (AGL) (Fig. 7a), a level at which particularly strong vertical displacements occur (cf. Fig. 6). CIN decreases on the downshear side of the vortex with a maximum reduction of 25 J kg^{-1}, which in this particular case eliminates up to 1/2 of the CIN present at the beginning of the simulation. On the upshear side of the vortex, the maximum increase in CIN of over 90 J kg^{-1} far exceeds the reduction on the downshear side. The decrease in CIN on the downshear side is concurrent with an increase in conditional instability, and the increase in CIN on the upshear side is concurrent with a decrease in conditional instability, with extrema of ΔCAPE of 650 and -950 J kg^{-1}, respectively. The negative correlation between ΔCAPE and ΔCIN results in thermodynamic conditions for strong convection based in the boundary layer becoming more (less) favorable with time downshear (upshear) of the vortex center.

At the location of the maximum 1.5-km downward displacement on the upshear side of the vortex (denoted by D in Fig. 7), cooling due to horizontal advection is slightly greater than warming from subsidence in the lowest 500 m, as evinced by the 8-h decrease of θ_e^* (equivalent potential temperature of a hypothetically saturated atmosphere) of $\sim$2 K (Fig. 8a). Above the boundary layer, strong warming from subsidence exceeds the cooling from horizontal advection associated with the vortex-induced northerly flow (cf. Fig. 7b), resulting in large increases in θ_e^* (Fig. 8a). Strong drying can be inferred by the small drop in θ_e above the boundary layer despite large θ_e^* increases.

A nonentraining boundary layer air parcel will conserve θ_e upon ascent and become positively buoyant if and when it reaches its LFC, where environmental θ_e^* becomes less than the parcel's conserved θ_e. Hence, the cold advection at low levels enhances CIN and reduces

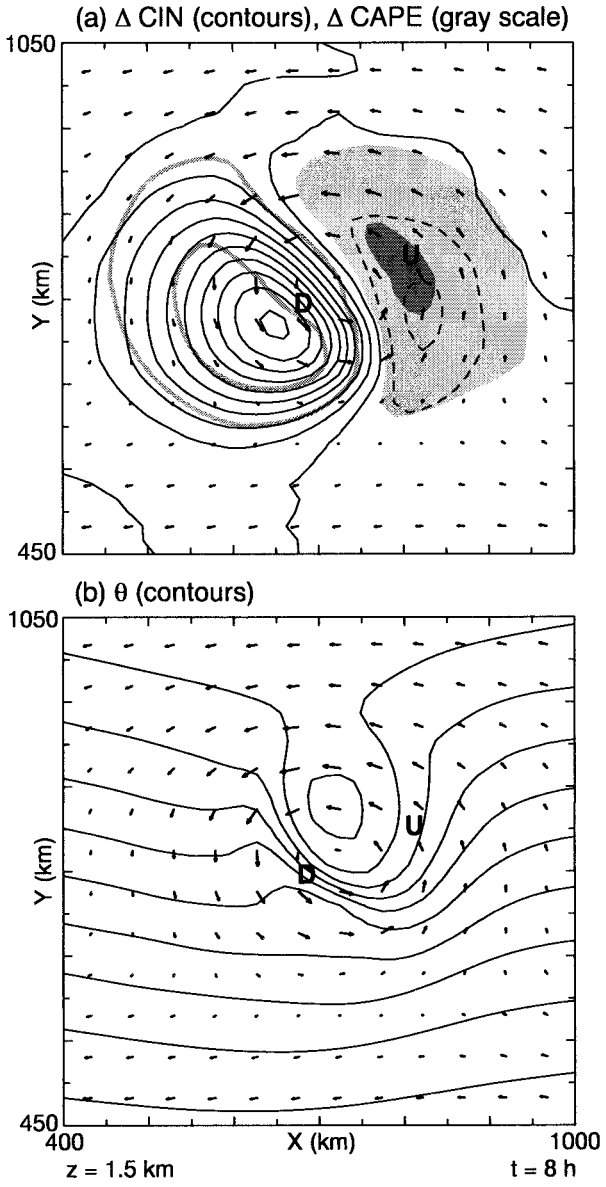

FIG. 7. The 1.5-km AGL system-relative vectors at 8 h, with (a) 8-h change in the CIN for the lowest 500 m AGL (10 J kg^{-1} contours, positive values solid, negative values dashed) and the 8-h change in CAPE for the lowest 500 m AGL [100–600 J kg^{-1} (light shading), $\geq$600 J kg^{-1} (dark shading), -100 and -600 J kg^{-1} contoured in gray] and (b) the 1.5-km potential temperature at 8 h (0.5-K contours). The annotations D and U denote the respective locations of the maximum downward and upward displacements from Fig. 6. Vectors are plotted as in Fig. 4.

conditional instability by lowering the average θ_e of the boundary layer by $\sim$1 K (Fig. 8a) while the subsidence warming above the shallow boundary layer even more dramatically increases CIN (Fig. 7a) and reduces conditional instability by contributing substantially to the 8-h rise in the LFC from 1.5 to 3.2 km (Fig. 8a).

At the location of maximum 1.5-km upward displacement downshear of the vortex center, large increases in

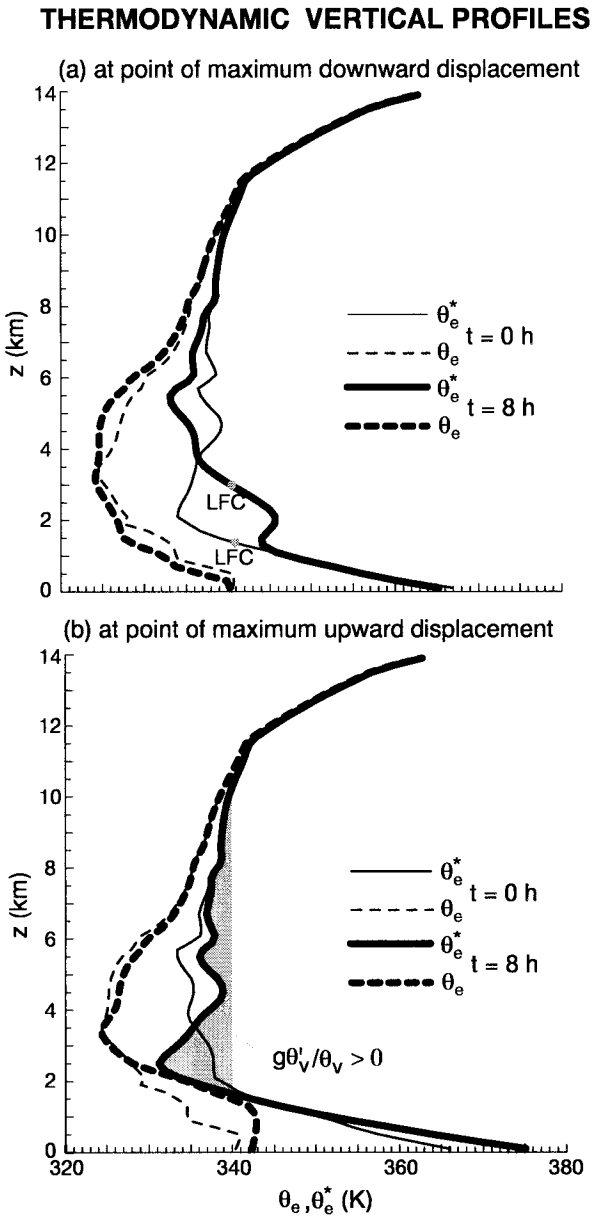

FIG. 8. Vertical profiles of equivalent (θ_e, dashed) and saturated equivalent (θ_e^*, solid) potential temperatures at 0 (thin) and 8 h (bold) at the locations of maximum time-integrated 1.5-km (a) downward and (b) upward displacement denoted by the respective annotations of D and U in Fig. 7. The LFC annotations in (a) refer to the level of free convection for an air parcel averaged over the lowest 500 m of the two soundings. The shading in (b) corresponds to the integrated positive buoyancy an air parcel from the lowest 500 m of the saturated layer of the latter sounding (t = 8 h) would experience upon moist-adiabatic ascent.

θ_e^* from low-level warm advection correspond to the ~2–3 K increase in boundary layer θ_e (Fig. 8b). This change in the boundary layer is the primary reason for increases in conditional instability, with a smaller contribution resulting from the cooling associated with ascent above the boundary layer. The lifting has also substantially deepened the boundary layer so that by 8 h, its top is within ~300 m of the LFC (Fig. 8b), and CIN (Fig. 7a) is accordingly reduced.

Although thermodynamic conditions for surface-based convection improve substantially over the 8-h period in the vicinity of strong upward displacements, the application of these results to actual cases of MCVs is limited by the lack of a diurnal cycle of radiation. In long-lived MCVs, organized convection is typically most prominent during the late evening and overnight, after which substantial cooling of the boundary layer has occurred. Thus, the greatest significance of the persistent vortex-induced mesoscale lifting may not be in increasing the conditional instability of the boundary layer (which itself may experience an overall decrease during the evening in actual cases), but rather its role in the saturation of the ~1 km deep layer above the boundary layer between 1.25 and 2.25 km (Fig. 8b). The air parcels that constitute the layer of strong upward displacement originate near the top of the boundary layer on the southeastern flank of the vortex 8 h earlier. In nature, such air parcels are likely to have high θ_e, since they originate along the periphery of the vortex where daytime midlevel cloudiness is less widespread than near its center, and are unlikely to experience significant subsequent nocturnal cooling since they remain elevated as they ascend toward the center of the vortex. These air parcels, located within the lowest 500 m of the elevated saturated layer at 8 h have average θ_e = 340 K, and are thus positively buoyant through much of the troposphere, as indicated by the shading in Fig. 8b. Unlike the air in the conditionally unstable boundary layer, the air in this saturated layer immediately above is absolutely unstable and does not require additional forcing for convection to occur.

The horizontal scale of the saturated absolutely unstable region above the boundary layer, and its location relative to the 1.5-km vertical displacements and the centroid of the vortex circulation, are shown in Fig. 9. The saturated region is approximately 125 × 125 km^2, with parcel theory predicting deep ascent of at least 6 km for the lowest 500 m of this layer over an area about 1/2 this size. At the level of the strong vertical displacements (1.5 km) the saturated air is located significantly northeast of the vorticity center. However, since the vortex tilts slightly to the north of downshear, the saturated air is located close to the vortex center at its level of maximum strength, z_m = 3.5 km, and slightly upshear of the vortex center at 5.5 km (Fig. 9).

The foregoing has established how persistent ascent associated with the interaction of the vortex circulation with environmental vertical shear, acting alone, can both enhance conditional instability of the environment over a mesoscale region in the vicinity of the vortex, and result in absolute instability over a smaller area near the vortex center by lifting to saturation the conditionally unstable air that originates along its downshear flank. However, the air remains significantly subsaturated

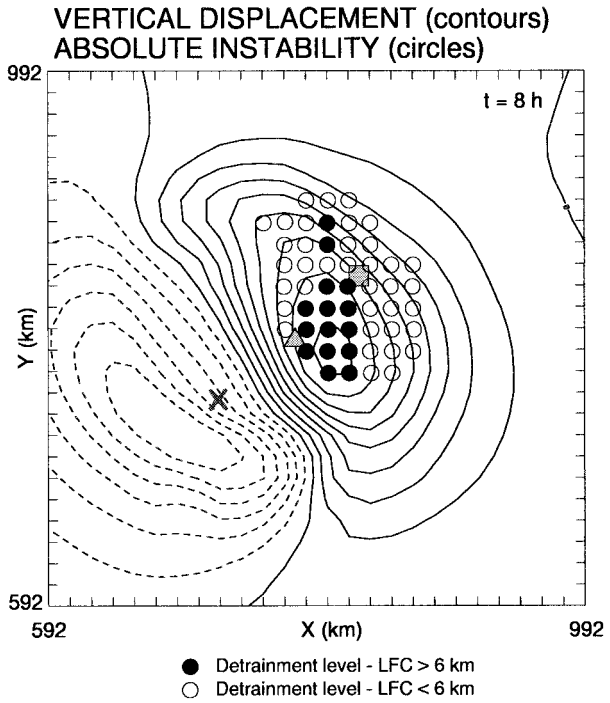

FIG. 9. Gridpoint locations of absolute thermodynamic instability in a saturated layer between 1.25 and 2.5 km AGL (circles) superposed on the vertical displacement field at 1.5 km AGL (100-m contour intervals, negative values dashed) for the control simulation V2R3S2 at 8 h. Solid (open) circles represent locations of deep (shallow) convective instability of this layer according to predictions from parcel theory. The symbols represent the locations of the vertical vorticity centroid at 1.5 (×), 3.5 (triangle), and 5.5 (square) km AGL.

along the downshear periphery of the vortex circulation. The interaction of the vortex with the ambient shear results in relatively modest decreases in CIN and increases in CAPE (Fig. 7a) in this location. Hence, additional forcing may be required to initiate the short-lived episodes of convection on the periphery of MCV circulations observed in Part I.

Aspects of the characteristics of thermodynamic destabilization in the current simulation are consistent with observations of secondary convective development in long-lived series MCV cases. The relatively small scale of the region of absolute instability is consistent with observations that outbreaks of secondary convection in association with MCVs are often smaller in scale than the parent MCS from which MCVs are spawned (cf. Fig. 11, Part I). The location of the absolute instability near the center of the vortex is consistent with observations of the location of long-lived secondary convection in Part I and with previous observational studies of series MCV cases (e.g., Fritsch et al. 1994). This location is optimal for MCV longevity, since the stretching of preexisting vertical vorticity that would occur in conjunction with secondary convection near the MCV center is likely necessary to sustain the vortex against environmental shear over long periods ($\tau > 12$–24 h).

4. Sensitivity to vertical shear and vortex parameters

In the absence of secondary convection, the most critical parameters governing vortex evolution are its aspect ratio, L/H, and the strength of the ambient vertical shear, $\partial u/\partial z$.[5] The ratio of these parameters, $(L/H)/(\partial u/\partial z)$, yields an approximate vortex timescale, $\tau \sim L/\Delta U$, where ΔU is the magnitude of the horizontal wind difference through the vortex depth. This favors vortex longevity for vortices of large horizontal scale and vortices occurring in weak ambient vertical shear. To make comparisons among vortices of different horizontal scale or among vortices in different vertical shear environments at similar stages of their evolution, we introduce the nondimensional time $t^* = t/\tau$. Here, the parameters L and ΔU in $\tau \sim L/\Delta U$ are represented, respectively, by the radius of maximum wind, r_m, and the magnitude of the vector difference in the horizontal flow between 0 and 6 km AGL (which itself is uniquely specified by the baroclinity parameter $\Delta\theta$ listed in Table 1).

One measure of the evolution of adiabatic vortices of a given horizontal scale is the degree of vertical tilt, which increases with time due to the presence of the vortex in a vertically sheared ambient flow. At the nondimensional time $t^* = 3.6$, which corresponds to the dimensional times of $t = 18$ h for the simulations V2R3S1 and V1R3S1 (strong and moderate vortices in weak shear, respectively) and $t = 6$ h for the simulation V1R3S3 (moderate strength vortex in strong shear), the vortices exhibit similar substantial vertical tilt (Fig. 10). The vortex tilt results in the clockwise rotation of the lower-tropospheric vertical motion couplet from its earlier orientation along the ambient vertical shear (shown for the control simulation in section 3a) for all simulations by $t^* = 3.6$. Lower-tropospheric vertical displacements (to be discussed shortly) are nearly maximized by this nondimensional time.

While the magnitudes of the vertical tilt are similar among these three simulations, there are significant differences in the orientations of the tilt, which themselves are influenced by both the initial vortex strength, V_m, and the strength of the ambient vertical shear, ΔU. The vertical tilt of the vortex remains oriented close to downshear in cases of weaker vortices in strong shear, unlike for stronger vortices in weak shear whose vertical tilt

[5] Variations in the ambient static stability can also effect evolution through corresponding variations in the vortex penetration depth (e.g., Jones 1995). However, warm-season variations in the tropospheric dry static stability are small compared with variations in vertical shear and are not considered in this section. While differences in lower-tropospheric vertical displacements are not anticipated to be strongly influenced by typical variations in the static stability, the reader is reminded that the extent to which such displacements may influence the development of secondary convection is crucially dependent on the moist thermodynamic stability.

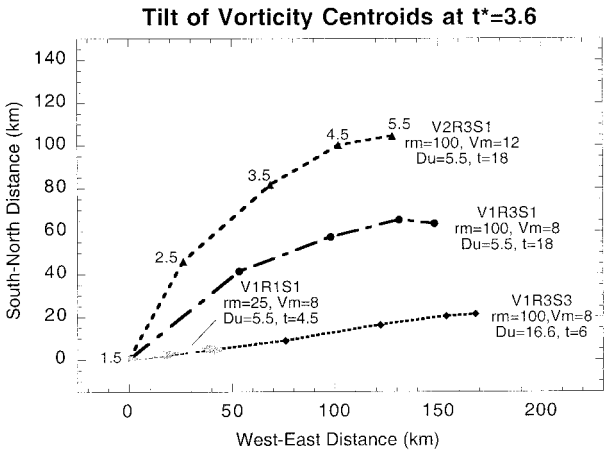

FIG. 10. Magnitude and orientation (in *x, y* plane) of the vertical tilt of the centroid of the vertical component of relative vorticity for simulations V2R3S1 (strong, large vortex in weak shear), V1R3S1 (moderate strength, large vortex in weak shear), V1R3S3 (moderate strength, large vortex in strong shear), and V1R1S1 (moderate strength, small vortex in weak shear) at nondimensional time $t^* = 3.6$. Symbols denote the locations of the vorticity centroid at 1-km height intervals from 1.5 to 5.5 km AGL as in Fig. 3.

becomes oriented significantly to the left of downshear (Fig. 10).

The simulation V1R1S1, initialized with a vortex four times smaller in horizontal extent than the simulations described above, displays a vertical tilt approximately 1/4 as large at the same nondimensional time (Fig. 10). However, this vortex is at a similar stage of evolution since its aspect ratio is equally smaller.

Like the orientations of vortex tilt (Fig. 10), the relationships between the instantaneous vertical velocity and the location of maximum vertical displacements vary significantly among the simulations depending on the relative strengths of the vortex and the ambient vertical shear. For instance, while the vertical motion pattern is similar for simulations V1R3S3 (moderate vortex in strong shear) and V2R3S1 (strong vortex in weak shear) at the same nondimensional time, the location of the 1.5-km upward displacements varies from nearly downshear of the vortex center for V1R3S3 (Fig. 11a) to almost 90° to the left (north) of downshear for V2R3S1 (Fig. 11b). The differences in the location of the strong vertical displacements are tied to the differences in air trajectories in the vicinity of the vortex, which themselves vary with $V_m/\Delta U$ (cf. Figs. 11a and 11b), and may influence where secondary convection is favored.

In addition to their locations, the strengths of the lower-tropospheric upward displacements relative to the vortex center vary significantly among simulations. Table 4 presents the maximum 1.5-km upward displacements (m) at $t^* = 3.6$ for the both the $V_m = 12$ m s^{-1} and $V_m = 8$ m s^{-1} matrices of simulations contained in Table 1. The larger and stronger vortices are clearly associated with the strongest maximum upward displacements, with some suggestion of an optimal value

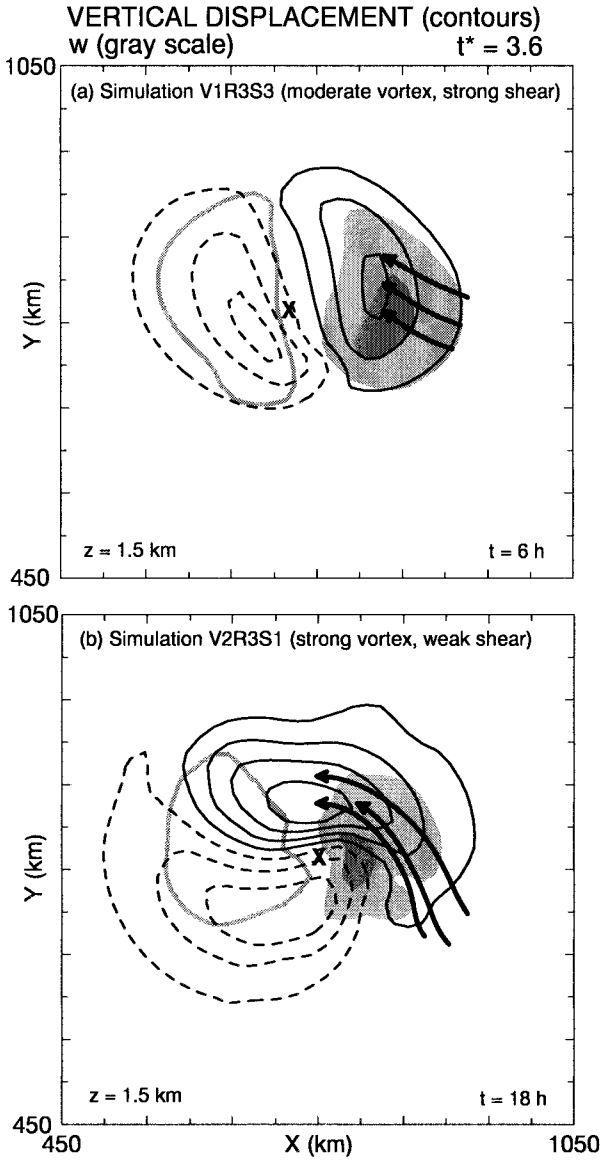

FIG. 11. As in Fig. 6a but for simulations (a) V1R3S3 (moderate vortex in strong shear) and (b) V2R3S1 (strong vortex in weak shear) at the nondimensional time $t^* = 3.6$.

TABLE 4. Maximum 1.5-km upward parcel displacements (m) as a function of vortex size r_m and vertical shear strength ΔU at nondimensional time $t^* = 3.6$ for the simulations with moderate ($V_m = 8$ m s^{-1}) and strong ($V_m = 12$ m s^{-1}) vortices listed in Table 1.

V_m (m s^{-1})	r_m (km)	[$\lvert\Delta U\rvert$ (0–6 km) m s^{-1})]		
		5.5	11.1	16.6
8	25	310	310	280
8	50	400	470	380
8	100	540	580	540
12	25	510	590	450
12	50	620	710	570
12	100	830	880	730

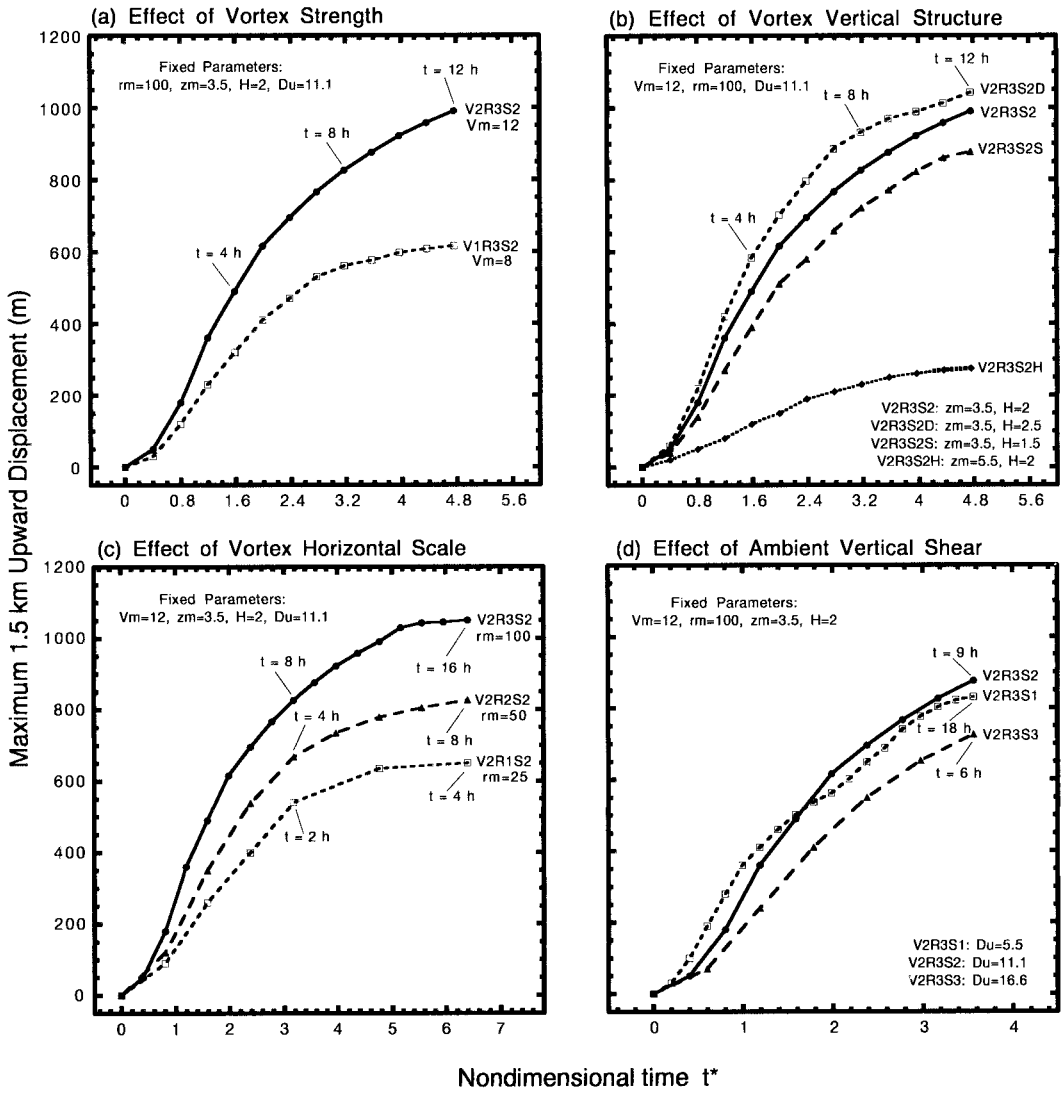

FIG. 12. Nondimensional time series plots of the maximum 1.5-km time-integrated upward displacements for simulations in which (a) vortex strength, (b) vortex vertical structure, (c) vortex horizontal scale, and (d) ambient vertical shear strength are varied. In (a) and (b), $L/\Delta U$ is constant among simulations so that a given nondimensional time corresponds to a single dimensional time. The symbols on the plotted curves indicate the dimensional time t at hourly increments, except in the case of simulation V2R1S2 of (c), where symbols denote t at half-hourly increments prior to $t = 2$ h ($t^* = 3.16$). In each panel the control simulation (V2R3S2) is denoted by the solid curve. Note the different scales among abscissas.

of ambient vertical shear near the midrange ($\Delta U = 11.1$). The control simulation (V2R3S2), which was initialized with a strong vortex of large horizontal scale in average ambient vertical shear, exhibits the strongest maximum upward displacements.

Stronger vortices produce greater upward displacements at all times (Fig. 12a). Unlike the vortex in the control simulation with $V_m = 12$ m s^{-1} (solid curve in Fig. 12a), a weaker vortex with $V_m = 8$ m s^{-1} (dashed curve in Fig. 12a) does not produce vertical displacements sufficient to saturate a part of the lower troposphere above the boundary layer at any time during the simulation for the specified composite sounding (Fig. 2).

The maximum upward displacements are also influenced by differences in the initial vertical structure (3) of the vortex. The top set of curves in Fig. 12b correspond to vortices centered at $z_m = 3.5$ km, but with different depth scales, H. The strongest lower-tropospheric vertical displacements are associated with the deepest vortices. Note that since the horizontal structure is the same in these three simulations, the deepest case (V2R3S2D), where $H = 2.5$ km, corresponds to a vortex with the greatest volume-integrated PV. The lower curve (V2R3S2H) represents the same initial vortex used in the control simulation (V2R3S2), but with its center raised from $z_m = 3.5$ to 5.5 km. Here, the vortex is

located largely above the layer of significant ambient vertical shear and produces weaker lower-tropospheric upward displacements (Fig. 12b). Unlike in the lower troposphere, maximum upward displacements above $z = 3$ km (not shown) in both the shallow and raised vortices are similar and at times exceed those associated with the deep vortex. However, a deep vortex that extends well into the lower troposphere will typically be most favorable for thermodynamic destabilization, since in most cases both the strongest vertical shear (which interacts with the vortex to produce the lifting) and the most unstable (high θ_e) air to be lifted are situated within the lowest few kilometers of the troposphere.

Figure 12c compares maximum 1.5-km upward displacements in simulations of vortices with differences in horizontal scale. Although at small t maximum upward displacements are largest in the rapidly evolving small vortex (V2R1S2), when plotted against nondimensional time t^*, the maximum upward displacements are always largest for the largest vortex (V2R3S2), with similar ratios between the maximum upward displacements among the different simulations for all t^*.

Back trajectories from the maximum 1.5-km upward displacement at $t^* = 3.16$ in V2R3S2 and V2R1S2 (not shown) have similar cyclonically curved paths that enter the instantaneous updraft pattern from the southern end and move northward relative to this pattern, which itself rotates anticyclonically (to the right of the ambient shear vector). The similarity in trajectories is not surprising because the maximum vortex tangential velocity ($V_m = 12$ m s^{-1}), and the ambient vertical shear ($\Delta U = 11.1$), are identical in these two simulations. The area of the updraft region scales approximately with the horizontal scale of the vortex (Fig. 13). Although the scale of the vertical velocity perturbation in the large vortex is four times that of the smaller vortex, its maximum instantaneous vertical velocity is only reduced from that of the smaller vortex by a factor of 2 during the steep portion of the trajectory ascent (Fig. 13). This suggests that the greater maximum 1.5-km upward displacement in the case of the large vortex can be attributed to a greater spatially integrated upward vertical velocity perturbation.

In addition to large vortices producing stronger upward displacements, for a given maximum upward displacement, large vortices will produce a vertical profile more favorable for the development of strong secondary convection at the location of maximum upward displacement. For example, the control simulation V2R3S2 ($V_m = 12$ m s^{-1}, $r_m = 100$ km) and simulation V2R2S2 ($V_m = 12$ m s^{-1}, $r_m = 50$ km) have nearly the same maximum 1.5-km upward displacement at $t = 8$ h. However, $t = 8$ h corresponds to a nondimensional time of $t^* = 6.32$ for the rapidly evolving smaller vortex versus $t^* = 3.16$ for the larger vortex of the control simulation (Fig. 12c). The vertical thermodynamic structure at the location of the maximum 1.5-km upward displacement in the simulations is accordingly different (Fig. 14). In

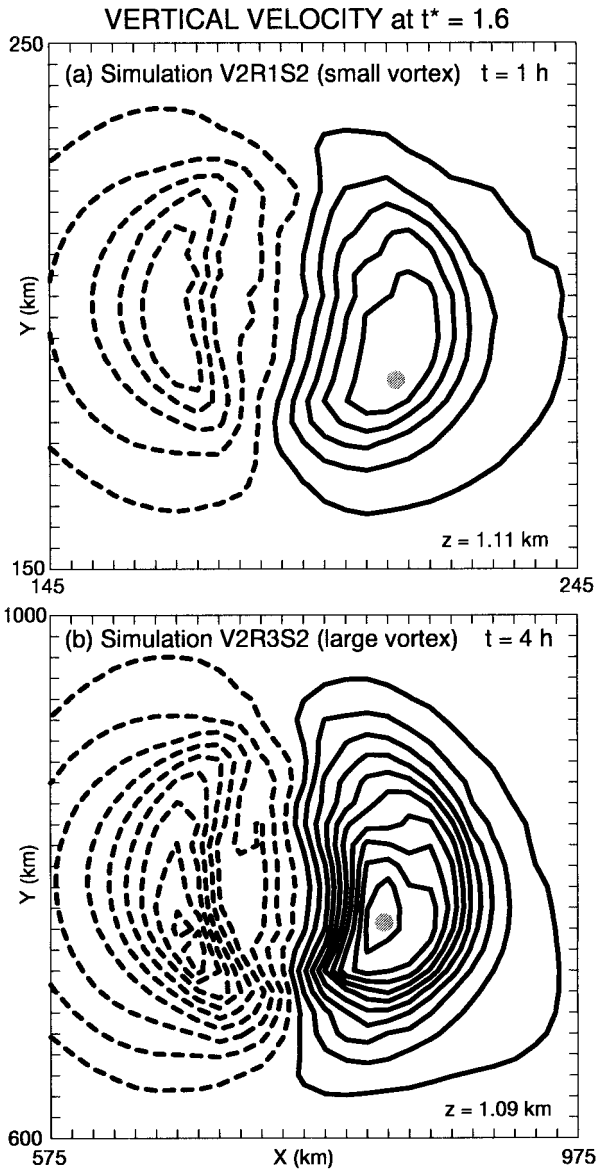

FIG. 13. Vertical velocity at nondimensional time $t^* = 1.6$ for simulations (a) V2R1S2 (small vortex, $r_m = 25$ km) at $z = 1.11$ km and (b) V2R3S2 (large vortex, $r_m = 100$ km) at $z = 1.09$ km. The display domain is scaled according to vortex size: (a) 100×100 km^2 and (b) 400×400 km^2. Vertical motion contours are (a) 2 cm s^{-1} and (b) 0.5 cm s^{-1}. Note that these different contour intervals are inversely proportional to vortex size. The dots indicate the corresponding locations at $t^* = 1.6$ of parcels from back trajectories taken from the position of maximum 1.5-km time-integrated upward displacement at $t^* = 3.6$ in each simulation.

both cases, the lower-tropospheric lifting has produced a saturated layer immediately above the boundary layer by $t = 8$ h.[6] However, for the smaller vortex, this layer is only ~400 m deep (Fig. 14a), instead of ~1000 m

[6] Unlike in the large vortex case, this layer is significantly subsaturated in the case of the smaller vortex at $t^* = 3.16$.

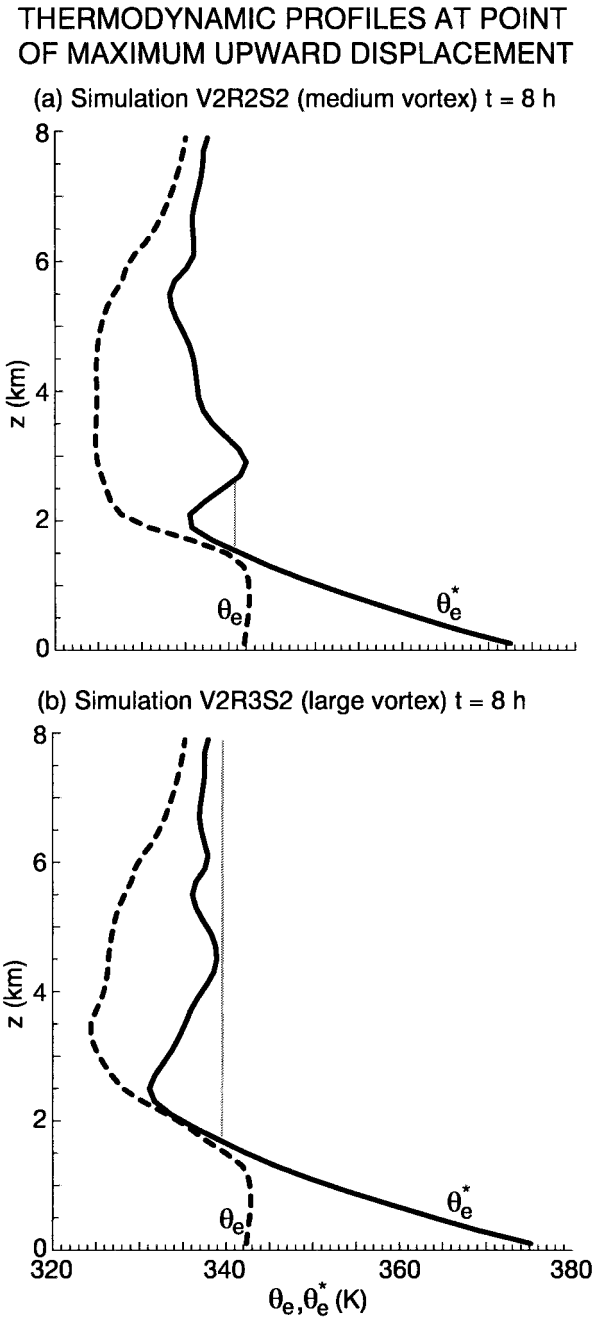

FIG. 14. Vertical profiles of equivalent (θ_e, dashed) and saturated equivalent (θ_e^*, solid) potential temperature at the locations of maximum time-integrated 1.5-km upward displacement for $t = 8$ h in simulations (a) V2R2S2 (medium-sized vortex) and (b) V2R3S2 (large vortex). The gray vertical lines indicate the depth of positive buoyancy for air parcels within the elevated absolutely unstable layer.

deep for the larger vortex (Fig. 14b). Moreover, deep convection of the most unstable air within the 400-m-deep layer is more likely to be adversely affected by the stable layer (evident from the θ_e^* inversion located above; Fig. 14a) in the case of the smaller vortex.

The reason for the differences in the θ_e^* profiles aloft

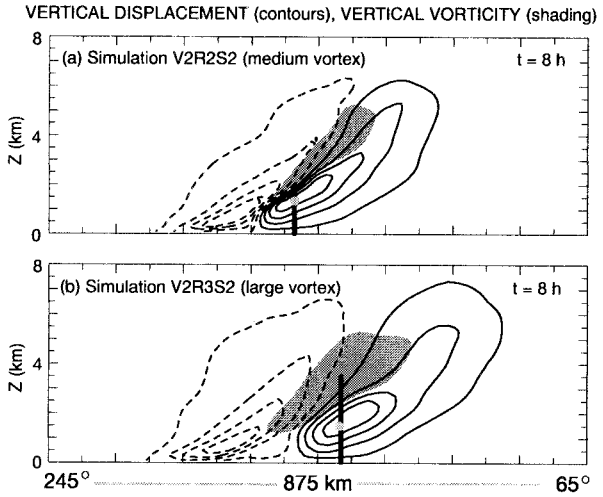

FIG. 15. Vertical cross section of the vertical component of the relative vorticity (shaded) and the vertical displacement (200-m contour intervals) through the maximum 1.5-km time-integrated upward displacement at $t = 8$ h (indicated by dotted symbol), along the approximate direction of the vertical tilt of the vortex for simulations (a) V2R2S2 (medium-sized vortex) and (b) V2R3S2 (large vortex). Shaded regions are (a) $\zeta \geq 6 \times 10^{-4}$ s^{-1} and (b) $\geq 1.5 \times 10^{-4}$ s^{-1}. The bold, vertically oriented line indicates the depth of upward displacement at the point of maximum 1.5-km upward displacement for which vertical thermodynamic profiles are displayed in Fig. 14.

(Fig. 14) is simply that the smaller aspect ratio (e.g., L/H) of the smaller vortex dictates that the warm, subsided air, centered approximately on its upshear flank (Fig. 15a), will more closely overlie the saturated unstable air centered approximately on its downshear flank than in the larger vortex (Fig. 15b), for vortices having the same vertical tilt. Large vortices are therefore more likely to be associated with thermodynamic destabilization not only because they produce more substantial maximum upward displacements but also because the depth of upward displacement over a given location is greater.

The relationship of the nondimensional time evolution of upward displacements among vortices in environments of differing vertical shear is more complicated than it is among vortices of different horizontal scale. For $t^* \leq 1.5$, maximum 1.5-km upward displacements are greater for ambient vertical shears representative of weakly sheared MCV environments ($\Delta U = 5.5$) than those representative of average environments ($\Delta U = 11.1$) (Fig. 12d). However, later in the simulation, the weakest shear environment produces slightly weaker maximum upward displacements than an environment of average shear does. Much stronger than average shear ($\Delta U = 16.6$) is suboptimal for producing 1.5-km upward displacements throughout the simulation (Fig. 12d).

5. Summary and discussion

In Part II of this study, idealized numerical simulations with a PE model have been used to examine the

interaction of MCVs with their environments. Our focus has been on how the mesoscale lifting associated with the interaction of an MCV with ambient vertical shear can thermodynamically destabilize the lower troposphere, as hypothesized by Raymond and Jiang (1990). This destabilization is expected to facilitate, and in some cases initiate, secondary convection in MCVs.

The numerical model is initialized using a vortex in gradient and hydrostatic balance superposed on a thermally balanced zonal jet that is representative of the large-scale weakly baroclinic condition of MCV environments observed in Part I. The ensuing vertical motion pattern consists of lower-tropospheric ascent on the downshear flank of the vortex with descent on the upshear flank, as in Raymond and Jiang (1990). Subsequent clockwise rotation of the vertical motion couplet is qualitatively consistent with predictions from quasigeostrophic theory and is interpreted as a balanced response to the vortex acquiring a vertical tilt, which itself is initiated by differential advection of the vortex in the ambient vertical shear.

The observations in Part I have guided an examination of the MCV-induced lifting and its associated thermodynamic destabilization properties over a broad range of ambient shear strengths and vortex characteristics, including initial vortex strength, horizontal scale, and vertical structure. The location of maximum vertical displacements in the lower troposphere is controlled by the relative strengths of the ambient vertical shear and the tangential velocity of the vortex circulation. The maximum upward displacements in the lower troposphere occur near the radius of maximum vortex winds and are located approximately downshear of the vortex center for vortices of moderate strength in relatively strong ambient shear, to as much as 90° to the left of downshear for strong vortices in relatively weak ambient shear. Since the simulated vortices develop significant vertical tilt, by the time substantial vertical displacements have occurred, the maximum lower-tropospheric upward displacements and resulting thermodynamic destabilization are located close to the center of the vortices at the level of maximum vortex strength. This location is consistent with observations that long-lived secondary convection within MCVs tend to occur near the MCV center. This location is optimal for reinvigoration of the vortex circulation (e.g., Ritchie and Holland 1997; Montgomery and Enagonio 1998), which may prolong its existence in a vertically sheared environment.

The simulations indicate that the lifting of conditionally unstable air to saturation is most likely to occur with strong vortices (e.g., $V_m \sim 12$ m s^{-1}) of moderate-to-large size (e.g., $r_m \geq 50$ km). Vortices of this horizontal scale are generally detectable from routine observations from the modernized operational weather network of the United States (Part I). Given identical ambient thermodynamic conditions, the time-integrated lifting by the larger vortices produces the most favorable thermodynamic structure for secondary convection. Vortices of only moderate strength (e.g., $V_m \sim 8$ m s^{-1}) may also produce a favorable thermodynamic structure for secondary convection. However, in these cases the simulations suggest that the lower troposphere would need to be exceptionally moist for the time-integrated lifting associated with weaker MCVs to be sufficient to produce saturation. The simulations also suggest that deeper MCVs that extend downward, well into the lower troposphere, are most favorable for thermodynamic destabilization since in the majority of cases both the strongest ambient vertical shear, which interacts with the vortex to produce the lifting, and the most conditionally unstable air to be lifted are concentrated within the lowest few km of the troposphere.

Observations presented in Part I indicate that secondary convection was more likely in MCV environments where the ambient vertical shear was less than the average for the entire MCV sample. Simulations presented herein suggest that lifting sufficient to produce saturation can occur throughout the entire range of observed ambient shears, given large and strong enough vortices. In as much as the environments in which MCVs develop and those they later move into are similar, one possible reason that long-lived secondary convection is associated with particularly weak ambient shear is that the scale of the vortices themselves tend to be smaller in strong shear (e.g., Weisman and Davis 1998). Smaller vortices, themselves, are found to be less favorable for deep vertical displacements.

The current simulations are idealized in that the initial conditions include horizontal temperature variations but no horizontal moisture variation and the ambient vertical shear is simplified by having no directional variation. The current simulations also lack surface friction that may significantly influence vertical motion in the lower troposphere. Despite these limitations and simplifications, the current simulations have illustrated the typical magnitudes of upward parcel displacements associated with the MCV–ambient shear interaction mechanism (e.g., Raymond and Jiang 1990; Raymond 1992) and have demonstrated how this interaction alone can result in thermodynamic destabilization sufficient to generate secondary convection for a subset of observed conditions. Confirmation of this lifting mechanism with detailed datasets awaits, and additional work with convection-resolving models is needed to understand how, once initiated, the secondary convection may feedback to affect the longevities of MCVs and the details of their life cycles.

With regard to the predictability of secondary convection in association with MCVs, this study is designed to examine the thermodynamic destabilization from forced lower-tropospheric ascent associated with a balanced vortex interacting with ambient vertical shear. Several additional factors not addressed in this study, such as the diurnal radiative cycle and greater complexity in the basic-state kinematic and thermodynamic

environment, are likely to influence when and where secondary convection associated with MCVs will occur. For example, observations from Part I indicated that a mode of short-lived secondary convection, which typically occurs earlier in the afternoon along the downshear periphery of the MCV circulation, may be as common as the typically longer-lived convection that occurs closer to the MCV center. The convection on the periphery of the MCV circulation cannot be explained solely by the lifting mechanism examined in this study, and may involve phenomena that are closely tied to the diurnal cycle, including the possible influence of thermally driven vertical circulations initiated by differential surface heating or, in some cases, additional forcing mechanisms such as cold fronts, drylines, and other planetary boundary layer disturbances. On the other hand, the forced lower-tropospheric ascent on the downshear flank of a vortex in ambient shear examined in this study may provide an explanation for the secondary convection that occurs closer to the MCV center. Such lifting may itself be modified in strength, and possibly location, by other factors including the larger-scale ascent associated with the nocturnal southerly low-level jet (e.g., Fritsch et al. 1994). The synergy of different effects in fostering an environment that allows regeneration of organized convection within the long-lived precipitation episodes associated with MCVs is the subject of ongoing study.

Acknowledgments. This research has benefited from discussions with Rit Carbone, Richard Rotunno, Gregory Hakim, and Tom Hamill (each of NCAR); Richard Johnson, Michael Montgomery, Jason Knievel (each of Colorado State University); and J. Michael Fritsch (The Pennsylvania State University). The authors are grateful to Andrew Crook (NCAR), Diana Bartels and David Blanchard (each of NOAA/NSSL), and the anonymous reviewers for their helpful reviews of this manuscript. This research is supported by a USWRP grant from NASA, NAG8-1510.

REFERENCES

Bartels, D. L., and R. A. Maddox, 1991: Midlevel cyclonic vortices generated by mesoscale convective systems. *Mon. Wea. Rev.*, **119,** 104–118.

Cotton, W. R., M.-S. Lin, R. L. McAnelly, and C. J. Tremback, 1989: A composite model of mesoscale convective complexes. *Mon. Wea. Rev.*, **117,** 765–783.

Davis, C. A., and M. L. Weisman, 1994: Balanced dynamics of mesoscale vortices produced in simulated convective systems. *J. Atmos. Sci.*, **51,** 2005–2030.

Frank, W. M., and E. A. Ritchie, 1999: Effects of environmental flow upon tropical cyclone structure. *Mon. Wea. Rev.*, **127,** 2044–2061.

Fritsch, J. M., J. D. Murphy, and J. S. Kain, 1994: Warm core vortex amplification over land. *J. Atmos. Sci.*, **51,** 1780–1807.

Jones, S. C., 1995: The evolution of vortices in vertical shear. I: Initially barotropic vortices. *Quart. J. Roy. Meteor. Soc.*, **121,** 821–851.

Maddox, R. A., 1983: Large-scale meteorological conditions associated with midlatitude, mesoscale convective complexes. *Mon. Wea. Rev.*, **111,** 1475–1493.

Montgomery, M. T., and J. Enagonio, 1998: Tropical cyclogenesis via convectively forced Rossby waves in a three-dimensional quasi-geostrophic model. *J. Atmos. Sci.*, **55,** 3176–3207.

Raymond, D. J., 1992: Nonlinear balance and potential-vorticity thinking at large Rossby number. *Quart. J. Roy. Meteor. Soc.*, **118,** 987–1015.

——, and H. Jiang, 1990: A theory for long-lived mesoscale convective systems. *J. Atmos. Sci.*, **47,** 3067–3077.

Reasor, P. D., M. T. Montgomery, F. D. Marks Jr., and J. F. Gamache, 2000: Low-wavenumber structure and evolution of the hurricane inner core observed by airborne dual-Doppler radar. *Mon. Wea. Rev.*, **128,** 1653–1680.

Ritchie, E. A., and G. J. Holland, 1997: Scale interactions during the formation of Typhoon Irving. *Mon. Wea. Rev.*, **125,** 1377–1396.

Skamarock, W. C., M. L. Weisman, C. A. Davis, and J. B. Klemp, 1994: The evolution of simulated mesoscale convective systems in idealized environments. Preprints, *Sixth Conf. on Mesoscale Processes*, Portland, OR, Amer. Meteor. Soc., 407–410.

Trier, S. B., C. A. Davis, and J. D. Tuttle, 2000: Long-lived mesoconvective vortices and their environment. Part I: Observations from the central United States during the 1998 warm season. *Mon. Wea. Rev.*, **128,** 3376–3395.

Weisman, M. L., and J. B. Klemp, 1984: The structure and classification of numerically simulated convective storms in directionally varying wind shears. *Mon. Wea. Rev.*, **112,** 2479–2498.

——, and C. A. Davis, 1998: Mechanisms for the generation of mesoscale vortices within quasi-linear convective systems. *J. Atmos. Sci.*, **55,** 2603–2622.

Wicker, L. J., and R. B. Wilhelmson, 1995: Simulation and analysis of tornado development and decay within in three-dimensional supercell thunderstorm. *J. Atmos. Sci.*, **52,** 2675–2073.